

3 THE TWO-DIMENSIONAL PROJECTED SPATIAL DISTRIBUTION OF GLOBULAR CLUSTERS: I. METHOD
4 AND APPLICATION TO NGC4261.

5 R. D'ABRUSCO¹, G. FABBIANO¹, J. STRADER², A. ZEAS^{1,3,4}, S. MINEO¹, T. FRAGOS¹, P. BONFINI³, B. LUO⁵, D.-W. KIM¹,
6 A. KING⁶

version February 27, 2024: fm

7 ABSTRACT

8 We present a new method for the determination of the two-dimensional (2D) projected spatial dis-
9 tribution of globular clusters (GCs) in external galaxies. This method is based on the K-Nearest
10 Neighbor density estimator of Dressler (1980), complemented by Monte-Carlo simulations to estab-
11 lish the statistical significance of the results. We apply this method to NGC4261, a “test galaxy”
12 where significant 2D anisotropy in the GC distribution has been reported. We confirm that the 2D
13 distribution of GC is not azimuthally isotropic. Moreover, we demonstrate that the 2D distribution
14 departs from the average GC radial distribution results in highly significant spiral-like or broken
15 shell features. Overall, the same perturbations are found in “red” and “blue” GCs, but with some dif-
16 ferences. In particular, we observe a central feature, roughly aligned with the minor axis of NGC4261,
17 composed of red and most luminous GCs. Blue and fainter GCs are more frequent at large radial
18 distances and follow the spiral-like features of the overall density structure. These results suggest a
19 complex merging history for NGC4261.

20 1. INTRODUCTION

21 A considerable body of work has been accumulated
22 in the past two decades on the properties of GCs pop-
23 ulations in elliptical galaxies (see review by Brodie &
24 Strader 2006). The studies available in the literature
25 that use both Hubble Space Telescope (HST) and larger
26 ground based telescopes, have established the existence
27 of red (metal rich) and blue (metal poor) subpopula-
28 tions of GCs in most galaxies. The radial distributions
29 of these populations differ, with the red/metal rich GCs
30 being more centrally concentrated than blue GCs. These
31 results suggest different formation scenarios for the two
32 GC subpopulations, which may reflect the formation his-
33 tory of their parent galaxy. Brodie & Strader (2006),
34 in particular, argue that blue GCs may have formed in
35 low-mass dark matter halos in the early universe, while
36 the red GCs were built in subsequent dissipative buildup
37 of the parent galaxy. Other studies have investigated
38 possible formation mechanisms for the families of low-
39 metallicity and high-metallicity GCs using different ap-
40 proaches. These studies include semi-analytical models
41 that use galaxy assembly history from cosmological sim-
42 ulations and observed scaling relations to estimate the
43 amount and metallicity of cold gas available for star for-
44 mation (Muratov & Gnedin 2010), physical models of the
45 collapse leading to the formation of GCs based on high

46 mass resolution simulations (Griffen et al. 2010), and
47 models based on the observed galaxy mass-metallicity
48 relation, the galaxy stellar mass function and theoret-
49 ical merger rates (Tonini 2013). Other authors have
50 explained the formation of low-metallicity GCs as star-
51 burst remnants of old dwarf galaxies that could have en-
52 tered the halos of spiral galaxies (Elmegreen et al. 2012).
53 While these works have explored multiple possible ex-
54 planation of the peculiar observational traits of the GC
55 populations, no agreement has yet been reached in the
56 literature.

57 While the spectral and photometric properties of GC
58 populations, as well as their radial distributions, have
59 been explored in depth, relatively little work has ad-
60 dressed their two-dimensional (2D) distributions (e.g.
61 NGC4471 in Rhode & Zepf 2001, NGC1399 in Dirsch et
62 al. 2003; Bassino et al. 2006, NGC3379, NGC4406 and
63 NGC4594 in Rhode & Zepf 2004, NGC4636 in Dirsch
64 et al. 2005, multiple galaxies in Hargis & Rhode 2012,
65 NGC3585 and NGC5812 in Lane et al. 2013). This type
66 of work requires to extract the entire GC population with
67 full or near-full coverage of the parent galaxy. Aug-
68 mented by kinematics of the GC systems and subsys-
69 tems (Strader et al. 2011 for M87; Blom et al. 2012 for
70 NGC4365), these studies are bringing forth a picture of
71 complex and diverse GC populations in elliptical galax-
72 ies, consistent with a history of gravitational interactions
73 and merging with neighboring galaxies.

74 Here we study the 2D GC distribution of NGC4261, for
75 which deep observations of the innermost region of the
76 galaxy, obtained with HST, are reported by Bonfini et al.
77 (2012) (hereinafter B+12). NGC4261 first came to atten-
78 tion because of the inhomogeneous spatial distribution of
79 its low-mass X-ray binaries (LMXBs), which suggested a
80 possible minor merger event (Zezas et al. 2003). Since a
81 number of these LMXBs were associated with GCs (Gior-
82 dano et al. 2005), the entire population of 718 GCs was
83 extracted and studied with HST, revealing an azimuthal
84 asymmetry in its distribution, which was attributed to

¹ Harvard-Smithsonian Astrophysical Observatory, 60 Garden Street, Cambridge, MA 02138, USA

² Department of Astronomy, Michigan State University, 567 Wilson Road, East Lansing, MI 48824-2320, USA

³ Physics Department and Institute of Theoretical and Computational Physics, University of Crete, 71003 Heraklion, Crete, Greece

⁴ Foundation of Research and Technology, 71003, Heraklion, Crete, Greece

⁵ Department of Astronomy & Astrophysics, 525 Davey Lab, The Pennsylvania State University, University Park, PA 16802, USA

⁶ Department of Physics & Astronomy, University of Leicester, Leicester, UK

85 past minor merging or interaction (B+12). Ferrarese et al. (1996) also reported boxy isophotes which support
86 the hypothesis of recent gravitational interaction experi-
87 enced by NGC4261.

88 Although the results of B+12 are convincing, our
89 more advanced analysis methods provide a clearer pic-
90 ture of the asymmetry and its statistical significance.
91 Here we report the re-analysis of the 2D distribution
92 of this GC population aimed at quantifying the reality
93 and shape of the spatial features in the 2D GC distri-
94 bution. We have used the K-Nearest Neighbor method
95 (KNN, Dressler 1980) to identify the 2D features, sup-
96 plemented by Monte-Carlo simulations to test their sta-
97 tistical significance. In Section 2 the data used in this
98 paper are described. The method and the results of the
99 its application to NGC4261 are discussed in Section 3.
100 Our findings are discussed in Section 4 and summarized
101 in Section 5.

103 2. DATA

104 We have used the B+12 catalog of GC positions and
105 properties, which lists 718 GCs, within the D_{25} ellipse
106 of NGC4261 (de Vaucouleurs et al. 1991). From this
107 sample, we have extracted color and magnitude based
108 subsamples. Figure 1 (left) shows the $V-I$ histogram
109 where blue ($V-I < 1.15$) and red ($V-I \geq 1.15$) GCs
110 are separated following B+12. These authors found that
111 $V-I=1.15$ is the color corresponding to the 50% prob-
112 ability of the GC to belong to either the red or the blue
113 subpopulations, assuming a two-Gaussians model of the
114 color distribution. However, as discussed in B+12, the
115 GC color distribution does not show the clear bimodality
116 typical of the GC color distribution in other early-type
117 galaxies (Brodie & Strader 2006; Peng et al. 2006). Fig-
118 ure 1 (right) shows the histogram of I magnitudes; we
119 arbitrarily define high luminosity (High L) GCs those
120 with $I < 23$ mag, and low luminosity (Low L) GCs those
121 with $I \geq 23$ mag. The $I < 23$ value used to separate
122 low-L from high-L GCs was set to obtain equipopulated
123 classes of sources (see Tab. 1). The density and residual
124 maps obtained for the luminosity classes defined using
125 $I < 23$ are described in Sec. 3.1. Figure 2 shows the
126 spatial distributions of GC positions in the plane of the
127 sky, where the azimuthal asymmetry in the 2D projected
128 GC distribution is evident. Table 1 lists the number of
129 GCs in each of the main samples used in the following
130 analysis. Changing the color and luminosity boundaries
131 (shaded regions in the plots in Figure 1) does not affect
132 our results. Details can be found in Section 3.2.

Table 1

Summary of the samples of GCs observed in NGC4261 used in
the paper. The number in parenthesis in the last column
represent the GCs fainter than $I=24$ which are not used to
produce the density and residual maps for Low-L GCs.

	N_{tot}	N_{red}	N_{blue}	N_{HighL}	N_{LowL}
NGC4261	718	306	412	316	402(84)

133 We have excluded from our analysis the central cir-
134 cular region with $r < 0.42'$ where incompleteness in the
135 detection of the GCs is substantial (B+12). We have
136 also excluded the undersampled regions outside the D_{25}
137 isophote (de Vaucouleurs et al. 1991).

138 3. THE ANALYSIS

139 For each of the GCs samples listed in Table 1, we have
140 determined the 2D spatial distributions by applying the
141 K-Nearest Neighbor (KNN) density estimator (Dressler
142 1980). This density is based on the *local* distribution
143 of GCs, i.e. on the distances of the closest GCs. For
144 each knot of a regular grid covering the region where the
145 density is to be determined, we measured the distance of
146 the K -th nearest neighbor GC (D_K) from the position
147 of the knot. We used this approach in order to have
148 density estimates even in the low density regions of the
149 GC distribution. The point-density is estimated as:

$$D_K = \frac{K}{V_D(D_K)} \quad (1)$$

150 where K is the index of the nearest neighbor used to
151 calculate the density; for example, for $K=5$ only the 5
152 GCs nearest to the grid knot are used. V_D is the volume
153 of the region within the distance D_K of the K -th nearest
154 neighbor from the point where the density is evaluated.
155 In the case of 2D spatial density, the volume $V_D = \pi \cdot$
156 d_K^2 is equivalent to the area of the circle with radius
157 equal to the distance of the K -th nearest neighbor. The
158 assumption behind this method is that the density is
159 locally constant. The uncertainty on the KNN density
160 scales with the square root of K , so that the relative
161 fractional error is:

$$\frac{\sigma_{D(K)}}{D(K)} = \frac{1}{\sqrt{K}} \quad (2)$$

162 The fractional accuracy of the method increases with in-
163 creasing K at the expense of the spatial resolution.

164 For each subsample, we have determined the 2D GC
165 surface density by using values of K ranging from 2 to
166 10. The density values have been calculated on a regu-
167 lar grid with spacing $\sim 0.0018^\circ$ ($\sim 6.5''$) and $\sim 0.0015^\circ$
168 ($5.4''$) along the R.A. and Dec. respectively, in order
169 to have the same number of knots covering the whole re-
170 gion of the sky occupied by the GC distribution along the
171 two coordinate axes. Different spacings along the R.A.
172 and Dec. axes yield similar results to those described in
173 the following. The density in the pixels overlapping the
174 boundaries of the area covered by the observations has
175 been weighted according to the fraction the area of the
176 pixel located within the observed region.

177 To assess the significance of features suggested by the
178 KNN density maps (hereafter “observed” density maps),
179 we performed Monte-Carlo experiments, by creating ran-
180 dom samples of GCs, each conforming to the observed ra-
181 dial density distribution of the relevant observed samples.
182 The simulated random samples contain the same num-
183 ber of GCs as the corresponding observed samples. The
184 simulated radial positions were randomly drawn from the
185 histogram of the observed radial distribution of GCs in-
186 tegrated over elliptical annuli with the same eccentricity
187 and position angle of the D_{25} isophote ($e=0.45$, de Vau-
188 couleurs et al. (1991)). Independently, the azimuthal dis-
189 tributions were extracted from a uniformly random dis-
190 tribution between 0° and 360° . With this prescription,
191 we do not need to determine a 2D model of the observed
192 GC distribution in NGC4261. We introduced a geomet-
193 rical correction on the expected number of GCs to take

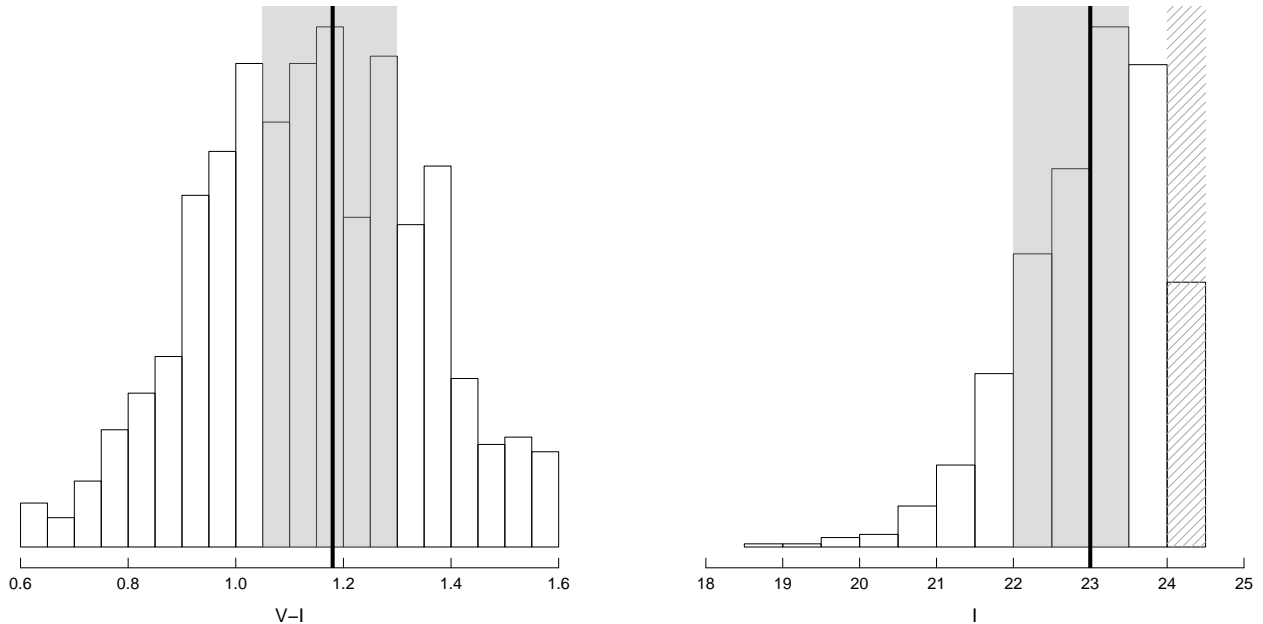


Figure 1. Left: Distribution of the $V-I$ color of the NGC4261 GCs sample. The vertical thick line ($V-I=1.15$) separates blue and red GCs, and the shaded gray area indicates the interval of color thresholds ($[1.05, 1.3]$) which determine density and residual maps for the two color classes qualitatively similar to the maps obtained with the ($V-I=1.15$) color threshold (see discussion in Sec 2 and Sec. 3.1). Right: Distribution of the I magnitude of the same sample. The vertical thick line separates high luminosity and low luminosity GCs and the shaded gray area indicates the interval of I magnitude value which determine density and residual maps similar to the maps obtained using the $I=23$ threshold (Sec. 3.1). The shading lines region for $I > 24$ has been not used to generate the density and residual maps for High-L and low-L GCs classes in Sec. 3.1.

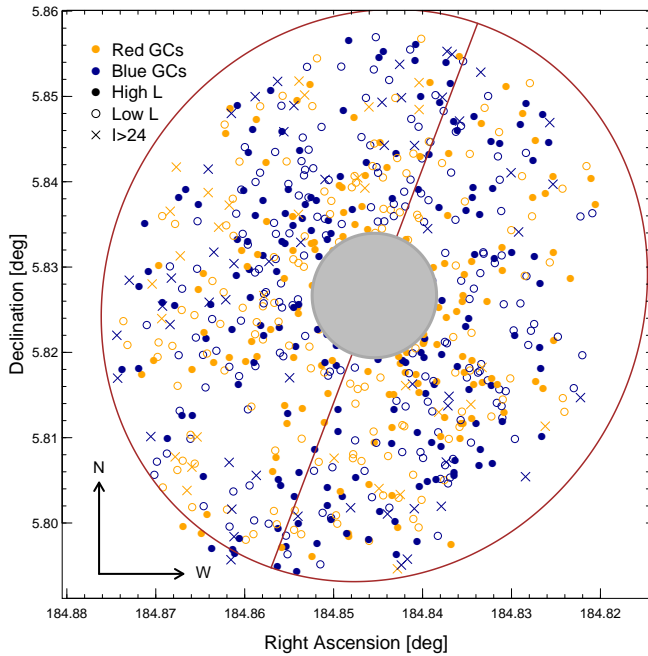


Figure 2. Positions of the GCs in NGC426. Blue and red GCs are indicated as blue and orange symbols. High-luminosity ($I \leq 23$) and low-luminosity GCs ($I > 23$) are indicated as solid and open symbols respectively, while the crosses represent GCs fainter than $I \geq 24$ that have been excluded from the luminosity classes analysis discussed in Section 3.1. The central gray area has been excluded from our analysis. The ellipse is the D_{25} isophote from de Vaucouleurs et al. (1991).

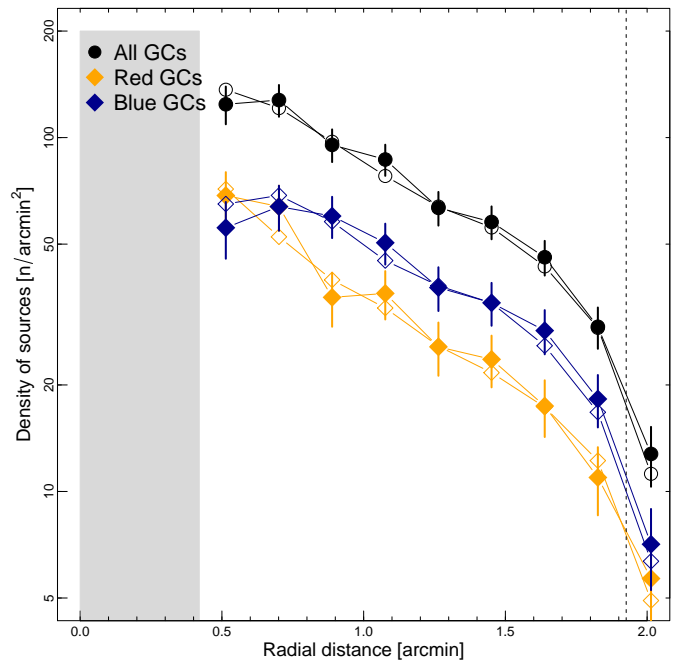


Figure 3. Observed (solid) and simulated (open) radial density profiles integrated in elliptical annuli for all (black symbols), red (orange symbols) and blue (blue symbols) GCs. The vertical dotted line marks the maximum radial distance of the D_{25} ellipse. The gray area has been excluded from our analysis.

194 into account the eccentricity of the galaxy.

195 We also tried using a histogram generated from the
196 best fit power law of the observed radial density profile
197 to seed our simulations. This approach has the advan-

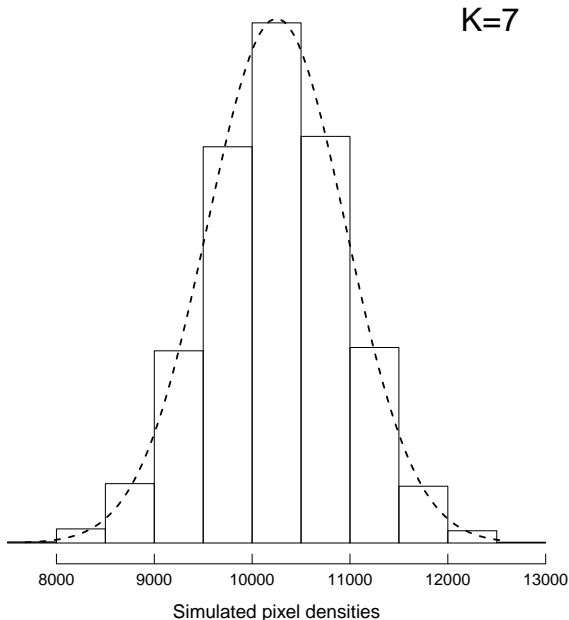


Figure 4. Representative histogram of the distributions of densities for a pixel of the density maps derived from the 5000 simulated spatial distributions of GCs for $K = 7$. The dashed line is the best-fit Gaussian model of the histogram.

198 tage of smoothing local density fluctuations and there-
 199 fore, in principle, makes us more sensitive to small-scale
 200 annular features. However, it introduces a model which
 201 may not represent the real radial distribution of GCs in
 202 NGC4261. Both approaches gave consistent results. In
 203 the following we will describe only the results obtained
 204 using the observed histogram to seed the simulations.

205 We performed 5000 simulations for each of the samples
 206 in Table 1 and constructed from each simulation the 2D
 207 density maps using the same KNN method applied to the
 208 observed data, for values of K ranging from 2 to 10. From
 209 these maps we derived average pixel-by-pixel simulated
 210 density maps for each sample under consideration (in the
 211 remainder of the paper, we will use “pixel” to indicate
 212 each cell in the R.A. vs Dec. grid used to evaluate the 2D
 213 density associated to the GCs spatial distribution). Fig-
 214 ure 3 compares the observed and simulated mean radial
 215 density profiles for the color-based samples.

216 Since our purpose is to characterize the deviations from
 217 the average radial trends of the GC distributions, our
 218 next step was to calculate the maps of residuals R by sub-
 219 tracting pixel-by-pixel the mean simulated density map
 220 $\langle S \rangle$ from the corresponding observed map O . These
 221 residual maps were also normalized by the value of the
 222 density in the average simulated map $\langle S \rangle$. The resid-
 223 ual R_i of the i -th pixel of the map is thus defined as:

$$R_i = \frac{(O_i - \langle S \rangle_i)}{\langle S \rangle_i} \quad (3)$$

224 We note that the pixel-by-pixel distributions of the
 225 simulated KNN densities are well approximated by Gaus-
 226 sians, simplifying the calculation of the statistical signif-
 227 icance of the observed over densities. A typical example
 228 of the pixel density distributions is shown in Figure 4.

229 To evaluate statistical significance of the observed

230 residuals, for each set of simulated density maps we cal-
 231 culated the fraction of pixels with values above the 90-th
 232 percentile of the densities in the observed maps (the “ex-
 233 treme” pixels).

234 Since the extreme pixels in the observed density and
 235 residual maps tend to be clearly spatially correlated, we
 236 also evaluated the fraction of simulations with at least
 237 one group of contiguous extreme pixels as large as the
 238 observed. For each simulation, we counted the number
 239 of groups of extreme contiguous pixels with area (mea-
 240 sured in pixels) equal to the area of the region within the
 241 density contours corresponding to the 90-th percentile
 242 observed density threshold. Since we did not impose any
 243 specific geometry to the groups of contiguous extreme
 244 pixels in the simulated density maps, these fractions rep-
 245 resent upper limits to the fraction of extreme contiguous
 246 pixels expected for a given spatial distribution of resid-
 247 als.

248 The results, compiled in Table 2, show that for small
 249 values of K , simulated density maps have a total fraction
 250 of extreme pixels larger than the observed. However,
 251 this fraction decreases with increasing K , and it becomes
 252 negligible for $K \geq 5$. The percentage of contiguous ex-
 253 treme pixels (in parenthesis in Table 2) does not exceed
 254 20% even for $K = 2$ and rapidly decreases to zero at
 255 $K = 5$. Therefore, the probability of a random distri-
 256 bution of high-density pixels with the observed spatial
 257 distribution is very low even for low K and becomes null
 258 with increasing K . Based on Table 2, in the following we
 259 will only discuss our results for $K \geq 5$. Figure 5 shows
 260 the histogram of the simulated number of extreme pix-
 261 els compared to the observed for $K = 9$ for the entire
 262 sample, and the corresponding histograms for spatially
 263 correlated extreme pixels. Together with Table 2, these
 264 comparisons shows that the degree of correlated features
 265 observed (discussed in detail below) in the data cannot
 266 be randomly produced.

3.1. Density and Residual maps

267
 268 Figure 6 shows the 2D KNN density maps for the spa-
 269 tial distribution of the entire GC sample for K ranging
 270 from 5 to 10. In all these maps two high-density struc-
 271 tures emerge in the S-W and N-E quadrants, on oppo-
 272 site sides of the galaxy major axis. The S-W density
 273 enhancement resembles a spiral arm and is composed
 274 of two distinct sections: a short elongated structure
 275 aligned along the radial direction and a second longer
 276 feature spanning azimuthally more than 45° . The N-E
 277 high-density region has an elongated shape and occu-
 278 pies azimuthally $\sim 100^\circ$. These over-densities roughly
 279 correspond to the local enhancements of the GC dis-
 280 tribution shown in Figure 9 of the B+12 paper, which
 281 was obtained by applying adaptive kernel smoothing and
 282 Voronoi Percolation-Tessellation. This figure shows that
 283 maps with $K = \{7, 8, 9\}$ are similar, while the $K = 10$
 284 maps smooth over some of the spatial features. In the
 285 remainder of the paper, we will discuss only the den-
 286 sity and residual maps obtained for $K = 9$ because these
 287 maps are the most statistically significant (as discussed
 288 in Section 3 and shown in Table 2).

289 We show in Figure 7 the $K = 9$ residual map, which
 290 highlights the existence of the two main over-densities
 291 in the S-E and N-W quadrants already observed in the
 292 density maps and discussed above, together with sim-

Table 2

Fractions of simulated density maps with number of extreme pixels (i.e., pixels with density values exceeding the 90-th percentile of the observed pixel density distribution) larger than the number of observed extreme pixels. Values in parenthesis refer to the fraction of simulated density maps with at least one group of contiguous extreme pixels as large as the groups of contiguous extreme pixels in the observed density maps (see details in Section 3). These fractions were determined by counting the number of simulated density maps with at least one group of contiguous extreme pixels equal or larger than the group of contiguous extreme pixels observed over-density regions.

NGC4261 (density)									
	$K=2$	$K=3$	$K=4$	$K=5$	$K=6$	$K=7$	$K=8$	$K=9$	$K=10$
All GCs (red+blue)	100%(12.4%)	100%(6.6%)	55.2%(0.9%)	0.2%(0%)	0%(0%)	0%(0%)	0%(0%)	0%(0%)	0%(0%)
Red GCs	100%(19.9%)	99.8%(12%)	20.8%(2.1%)	0.2%(0%)	0%(0%)	0%(0%)	0%(0%)	0%(0%)	0%(0%)
Blue GCs	100%(17.3%)	100%(9.8%)	77.4%(1.3%)	3.2%(0%)	0%(0%)	0%(0%)	0%(0%)	0%(0%)	0%(0%)
NGC4261 (residual)									
	$K=2$	$K=3$	$K=4$	$K=5$	$K=6$	$K=7$	$K=8$	$K=9$	$K=10$
All GCs (red+blue)	100%(4.4%)	100%(0.5%)	55.2%(0.1%)	0.2%(0%)	0%(0%)	0%(0%)	0%(0%)	0%(0%)	0%(0%)
Red GCs	100%(3.9%)	99.8%(1.4%)	20.8%(0%)	0.2%(0%)	0%(0%)	0%(0%)	0%(0%)	0%(0%)	0%(0%)
Blue GCs	100%(1.3%)	100%(0.2%)	77.4%(0.2%)	3.2%(0%)	0%(0%)	0%(0%)	0%(0%)	0%(0%)	0%(0%)

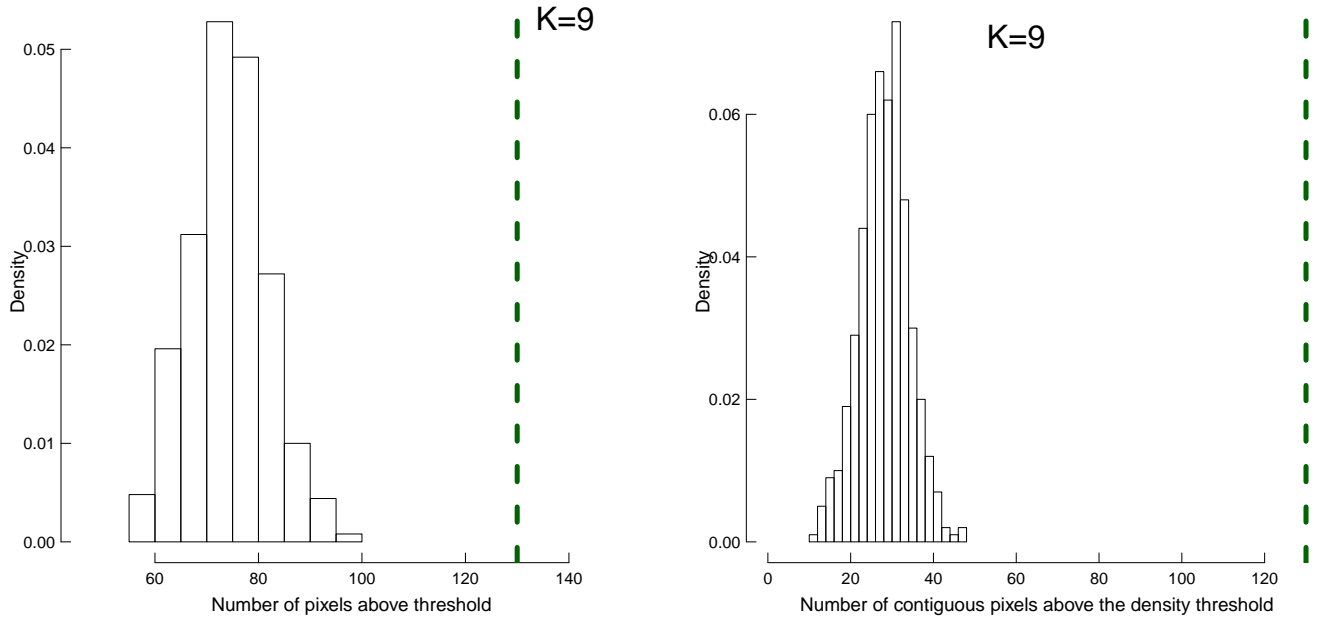


Figure 5. Left: histograms of the number of pixels in the simulated two-dimensional GCs density maps of the entire GC sample (calculated for $K=9$) with density $>$ 90-th percentile of the distribution of pixels in the observed density map. Right: same as above, with the additional constraint of spatial correlation as strong as the high-density pixels in the observed maps. In both plots, the vertical lines represent the number of observed pixels whose density exceeds the density thresholds.

293 ilarly significant under-densities in the S-E region and
 294 the western region of the galaxy. The latter is partially
 295 due to the incomplete HST coverage, see Figure 1 in
 296 B+12 for details. Figure 8 maps the single pixels with
 297 significance larger than 1σ , 2σ and 3σ . In particular the
 298 S-W features stands out, since multiple spatially corre-
 299 lated nearby pixels with significant positive residuals are
 300 located in this region. Although the N-E over-density
 301 is weaker, the spatial correlation of the pixels with posi-
 302 tive residuals in this case cannot be due to chance, as
 303 shown in Table 2. The number of GCs located within the
 304 pixels associated to positive residuals is 175 ($\sim 24\%$), 86
 305 ($\sim 12\%$) and 60 ($\sim 8\%$) for 1σ , 2σ and 3σ respectively.
 306 Table 3 shows the fractions of GCs located within the
 307 statistically significant over-densities for all GCs classes
 308 used in this paper.

309 Tal et al. (2009) report the presence of two low sur-
 310 face brightness structures, a NW tidal arm and a faint SE
 311 “fan” in NGC4261. These structures are located within
 312 the HST observations used by B+12 to extract the cat-

313 alg of GCs, but within the central avoidance region not
 314 used in this study (see Section 2). We have compared the
 315 spatial distribution of this faint optical features with the
 316 large scale shape of the GCs distribution in the region of
 317 the galaxy closest to the avoidance region, but we have
 318 not noticed any resemblance or clear correlation between
 319 the two different structures.

320 The $K=9$ maps of red and blue GC classes (Sec-
 321 tion 2), show significant differences in the over-densities,
 322 although the overall residuals follow those of the entire
 323 sample (Figure 9). In particular, a stronger concentra-
 324 tion of $\geq 3\sigma$ over-dense pixels can be seen in the north of
 325 the blue GC residual map. These results do not depend
 326 on the value of the B+12 color threshold used to define
 327 blue and red subpopulations, as long as the threshold is
 328 chosen within the interval $V-I = [1, 1.3]$. The density
 329 and residual maps of the two color classes using ten reg-
 330 ularly spaced threshold values in the above interval are
 331 self consistent. For values outside this interval, the signif-
 332 icance of the residual map for one of the classes degrades

Table 3

Number of GCs located in over-densities regions with significance larger than 1σ , 2σ and 3σ respectively for all classes of GCs used in this paper. In parenthesis, the percentage relative to the total number of sources in each class, as shown in Tab. 1.

	All GCs			Red GCs			Blue GCs		
	1σ	2σ	3σ	1σ	2σ	3σ	1σ	2σ	3σ
$K=5$	241(33.5%)	137(19.1%)	78(11.0%)	203(66.3%)	109(35.6%)	79(25.8%)	191(46.4%)	100(24.3%)	67(16.3%)
$K=6$	241(33.5%)	133(18.5%)	80(11.1%)	217(70.9%)	109(35.6%)	79(25.8%)	219(53.2%)	117(28.4%)	60(14.6%)
$K=7$	247(34.4%)	125(17.4%)	88(12.3%)	210(68.6%)	122(38.9%)	80(26.1%)	228(55.3%)	125(30.3%)	70(17.0%)
$K=8$	247(34.4%)	133(18.5%)	79(11.0%)	218(71.2%)	141(46.1%)	93(30.4%)	225(54.6%)	112(27.2%)	76(18.4%)
$K=9$	252(35.1%)	137(19.1%)	90(12.5%)	211(70.0%)	128(41.8%)	91(29.7%)	230(55.8%)	126(30.6%)	63(15.3%)
$K=10$	274(38.1%)	140(19.5%)	93(13.0%)	220(71.9%)	135(44.1%)	78(25.5%)	224(54.4%)	143(34.7%)	77(18.7%)
	High-L GCs			Low-L GCs					
	1σ	2σ	3σ	1σ	2σ	3σ			
$K=5$	194(61.4%)	104(33.0%)	58(18.3%)	200(62.9%)	103(32.4%)	73(23.0%)			
$K=6$	210(66.5%)	104(33.0%)	63(19.9%)	208(65.4%)	123(38.7%)	86(27.0%)			
$K=7$	216(68.4%)	107(33.9%)	55(17.4%)	221(69.5%)	138(43.4%)	96(30.2%)			
$K=8$	232(73.4%)	113(35.8%)	64(20.3%)	239(75.1%)	146(45.9%)	80(25.2%)			
$K=9$	231(73.1%)	112(35.4%)	67(21.2%)	262(82.4%)	142(44.7%)	98(30.8%)			
$K=10$	220(69.6%)	127(40.2%)	66(20.9%)	245(77.1%)	138(43.4%)	93(29.2%)			

333 rapidly because of the small number of GCs.

334 The observed radial density profiles of the GC distri-
335 butions in wedges aligned along the axes of the galaxy
336 (Figure 10) indicate that GCs have different radial distri-
337 butions along the directions of the major and minor axes
338 of the galaxy. The density profile of the entire sample
339 along the major axis is flatter than the average density
340 profile for radii $r \geq 1.2'$, while the minor axis density
341 profile is significantly steeper (Figure 10, left), after cor-
342 recting for geometrical effects. Both red and blue GC
343 profiles are more extended along the major axis, com-
344 pared with the minor axis distributions. This difference
345 is more striking for the blue GCs, which have a flat ma-
346 jor axis profile while the minor axis profile first increases
347 at small radii, and then plummets towards D_{25} .

348 The $K=9$ density maps for the high and low luminos-
349 ity subsamples (Table 1) are shown in Figure 12. The
350 density distributions show that the high-L GCs are more
351 centrally concentrated than the low-L ones. This is also
352 reflected by the azimuthally averaged radial profiles (Fig-
353 ure 11). This effect could be at least in part due to
354 incompleteness that will be more pronounced in the in-
355 ner radii where the galaxy stellar light is more intense.
356 Although there is a small radial dependence, this effect
357 is minimized by only using GCs with $I \leq 24$ for which,
358 according to B+12, a completeness of 75% is achieved.
359 However, there are azimuthal differences at the same ra-
360 dius that cannot be due to incompleteness effects. Fig-
361 ure 13 (lower panels) shows the position of the pixels with
362 residuals larger than 1σ obtained using $K=9$ for high-L
363 and low-L GCs (the same plots for blue and red GCs are
364 shown in the upper panels of Figure 13 for reference).
365 These plots also show significant differences: there is an
366 excess of High-L GCs to the W of the major axis in the
367 N, while the Low-L GCs present an excess to the opposite
368 SE side. The same conclusions about the spatial distri-
369 butions of low and high luminosity classes of GCs can
370 be drawn using different values of the threshold magni-
371 tude within the interval $I = [22, 23.5]$, using ten regularly
372 spaced magnitude thresholds. The High-L GCs are, in
373 each case, more centrally concentrated than Low-L GCs,
374 and High-L residuals show a unique significant positive
375 density enhancement in the N-W region of the galaxy.
376 Other values of the I magnitude have not been consid-
377 ered because they would generate luminosity classes too
378 unbalanced to correctly estimate the significance of the

379 results.

380 3.2. Color vs Spatial distribution of GCs

381 Blom et al. (2012) found significant effects in the color
382 vs galactocentric distance distribution of the GC system
383 of the galaxy NGC4365. We have investigated if simi-
384 lar effects are present in NGC4261. We have produced
385 the density maps of the distribution of GCs in the ra-
386 dial distance vs $V-I$ color with the KNN method for
387 $K = \{5, 6, 7, 8, 9, 10\}$. The map for $K=9$ is shown in Fig-
388 ure 14. The clumpy distribution of over-densities does
389 not show clear separation between different classes of
390 color except for a tendency of red GCs to be more cen-
391 trally concentrated than blue GCs, in agreement with
392 the density and residual maps of the two separate color
393 classes of GCs (Figure 9). In particular, at large radial
394 distances, the only interesting density enhancement of
395 Figure 14 is located in $r \sim 1.75'$ and $V-I \sim 1.12$. This
396 feature corresponds to the sum of the two significant den-
397 sity enhancements in the spatial density map of the blue
398 GCs class located along the major axis of the galaxy in
399 the N-W quadrant and in the S-W quadrant (see upper
400 left plot in Figure 9). A more detailed representation
401 of the GCs color distribution in NGC4261 as a function
402 of the position in the galaxy can be seen in Figure 15,
403 where each pixel is colored according to the average color
404 of the GCs placed within the pixel. The size of the pixels
405 is proportional to the density evaluated with the KNN
406 method for $K=9$ and the density contours are derived
407 from the same density map. Figure 15 confirms that red
408 and blue GCs tends to follow the same overall spatial
409 patterns, except for the different small differences visi-
410 ble in the upper panels in Figure 9, obtained using the
411 $V-I = 1.18$ color threshold value.

412 4. DISCUSSION

413 Our study of the 2D projected distribution of GCs in
414 the elliptical galaxy NGC4261 by means of KNN den-
415 sity maps has confirmed at high statistical significance
416 the presence of the 2D large-scale anisotropy reported
417 by B+12. The morphology of this anisotropy suggests a
418 large-scale spiral-like over-density which originates along
419 the major axis and follows the D_{25} elliptical isophote in
420 the periphery of the galaxy. Alternatively, there may be
421 a system of broken shells enclosing the major axis in both
422 directions roughly along the D_{25} ellipse, with local den-
423 sity enhancements especially along the northern segment

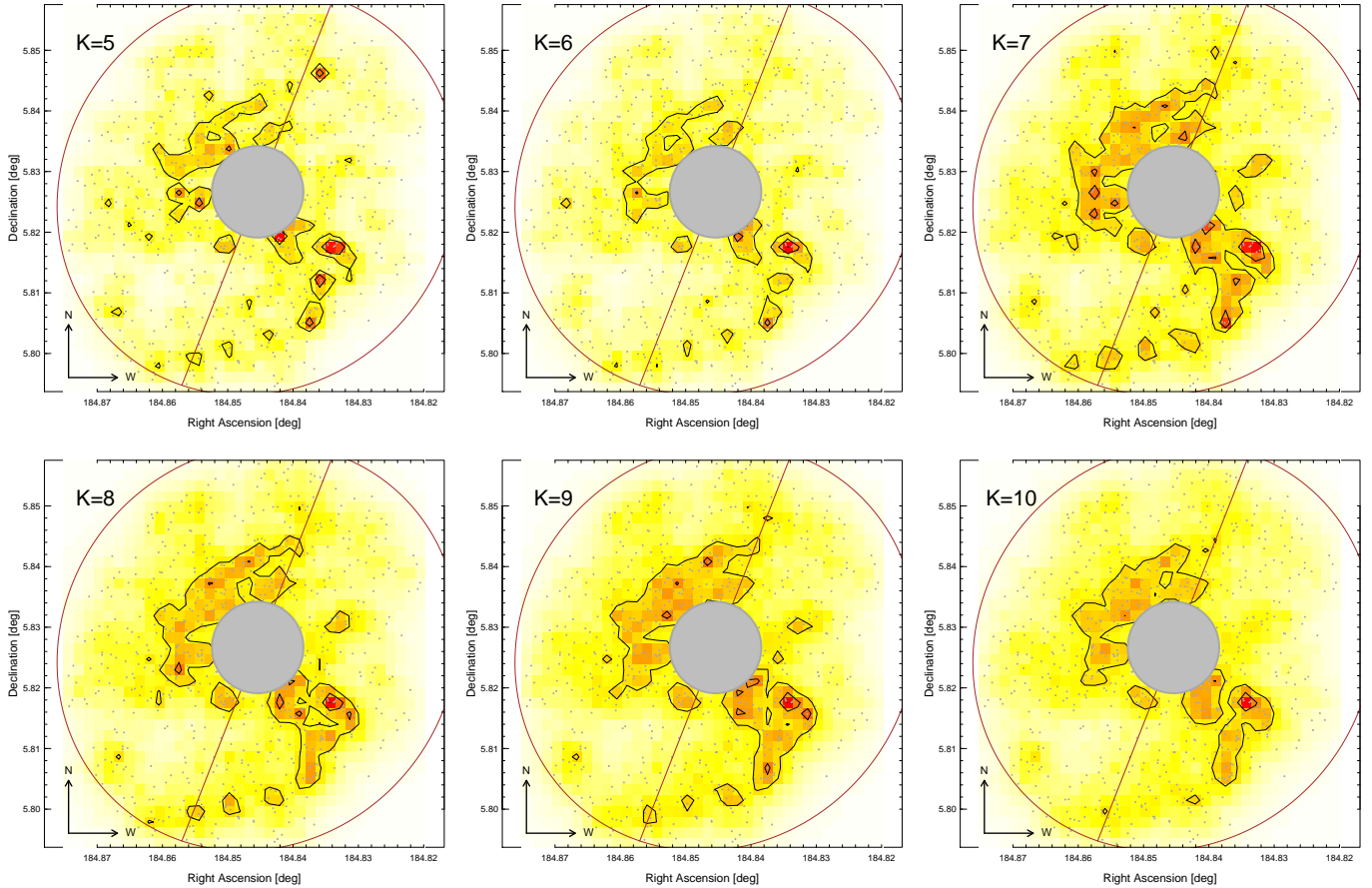


Figure 6. KNN density maps of the entire GC sample of NGC4261. Arbitrary isodensity contours show the higher-density regions in each map.

424 of the galaxy major axis. We find the same overall “grand
 425 pattern” when the sample is subdivided by either color
 426 or luminosity, although there are specific differences be-
 427 tween the subsamples. In particular, while the southern
 428 feature is seen in both red and blue GCs, the northern
 429 anisotropy shows some segregation of red and blue GCs.
 430 Similarly the morphology of the residuals differs in the
 431 N-W (see Section 3.1) suggesting a lack of high-L GCs
 432 in the inner major axis. Overall there are more red GCs
 433 at smaller radial distances (see Figure 3). However, we
 434 note that these effects may be correlated, since the high-
 435 L sample has a slightly larger fraction ($\sim 56\%$) of blue
 436 GCs (see Table 1).

437 At small radial distances, the density enhancements of
 438 the GCs distribution are aligned along the minor axis of
 439 the galaxy. The overall distribution is driven by high-
 440 L GCs which are located along the minor axis direction
 441 while low-L GCs do follow the broken-shell/spiral arm
 442 features more closely. These results differ significantly
 443 from recent results from Wang et al. (2013), which show
 444 that GCs of the early-type galaxies in the ACS Virgo
 445 Cluster survey tend to be aligned along the major axis in
 446 galaxies with visible elongation and intermediate to high
 447 luminosity. The GCs system in NGC4261 shows that the
 448 geometry of the GC distribution observed in the Wang
 449 et al. (2013) sample is not universal, even though the
 450 different conclusions based on the results provided by
 451 our method may depend on the rich sample of NGC4261

452 GCs used which, nonetheless, does not cover the whole
 453 GCs system.

454 As already discussed in B+12, these large-scale fea-
 455 tures suggest global shaping events, however their na-
 456 ture is not clearly understood. Tidal tails and shell-like
 457 ripples of the stellar surface brightness have been re-
 458 ported in several elliptical galaxies, and have been mode-
 459 led in terms of mergers and interactions with satellites
 460 (e.g., Schweizer 1980; Quinn 1984; Hernquist & Quinn
 461 1988, Hernquist & Quinn 1989). However, these simula-
 462 tions did not address GC systems.

463 In NGC4261, no significant sign of perturbation of the
 464 stellar surface brightness of the galaxy (except for two
 465 faint central structures noticed by Tal et al. 2009), is ob-
 466 served, indicating that a major merging event has not
 467 likely occurred in the last ~ 1 Gy. However, Ferrarese
 468 et al. (1996) observed boxy isophotes which are consis-
 469 tent with past merger. As discussed in B+12, a major
 470 merger scenario may be an alternative for the global 2D
 471 anisotropy of the GC distribution only if the relaxation
 472 timescale for the GCs is larger than that of the stars. An-
 473 other possibility in the major merger scenario is that the
 474 GC over-densities may be related with GC formed dur-
 475 ing the merger in shocked regions and tidal tails, such
 476 as the the evolved remnant of the young massive cluster
 477 populations detected in the Antennae (Whitmore et al.
 478 2010) and NGC 7252 (Bastian et al. 2013).

479 The peculiar spatial distribution of GCs in NGC4261

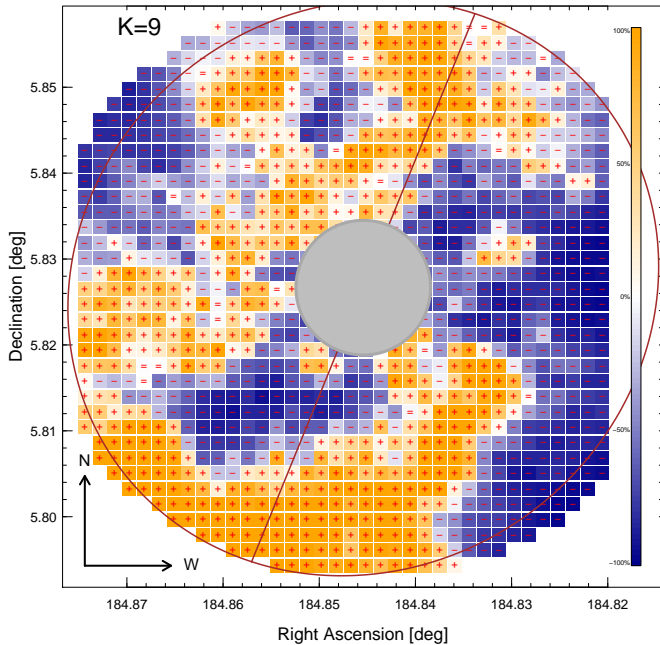


Figure 7. $K=9$ residual map of the entire GCs sample. Pixels are color-coded according to the number of σ the pixel deviates from the average. Darker colors indicate larger residuals: blue, negative; orange, positive. The small +, - and = signs within each pixel indicate positive, negative or null residuals respectively.

could also partially be influenced the GC systems of the smaller galaxies visible in the NGC4261 field and observed by Tal et al. (2009). In particular, two dwarf galaxies are visible in the HST images of NGC4261 GCs. The first, with $B = 16.2$ mag (Binggeli et al. 1985), is located in the N-W corner of the HST mosaic (R.A. = 12 : 19 : 17.6, Dec. = +5 : 52 : 39) and is too far from NGC4261 to contribute to the NGC4261 GCs system. The second ($B = 15.3$) is close to the S-W spiral-arm feature visible in the density map of the NGC4261 GCs system (R.A. = 12 : 19 : 23, Dec. = +5 : 47 : 51). Similar galaxies have compact GCs systems (see (Dirsch et al. 2005)). Thus, if this galaxy has an GCs system overlapping with the NGC4261 GCs population, this would only influence a small region of the spiral-like over-density associated to the NGC4261 GCs spatial distribution.

A third, brighter, galaxy ($B = 13.8$) (R.A. = 12 : 19 : 35, Dec. = +05 : 50 : 47), could in principle have a GCs population spatially overlapping the NGC4261 GCs system. Nonetheless, we notice that this galaxy is located on the E side of NGC4261 and no significant density enhancements is visible in the E outskirt of NGC4261 (Figure 6). A feature resembling a broken shell is apparent in the E quadrants of the NGC4261 closer to the center of the galaxy. Assuming a power-law radial density profile for the GCs system of the companion galaxy, the result of its contribution to the NGC4261 GCs density map would be an enhancement of the density decreasing from the outskirt to the center of NGC4261. For this reason, the contamination from the GCs system of the neighboring galaxy could only reduce the significance of the observed over-density in the E side of NGC4261, and would not change qualitatively the results of our analysis.

We cannot exclude that present and past gravitational

interactions with these neighboring galaxies may have affected the GC system of NGC4261, but the molding of these effects is beyond the scope of this paper.

Recent SPH simulations of the formation of GCs in merging and interactive galaxies suggest that newly formed metal-rich GCs tend to concentrate at the center of the merger remnant elliptical galaxy while metal-poor GCs are distributed in the outer parts due to strong angular momentum transfer (see Bekki et al. 2002). However, our residual maps, while showing a few differences in the over-densities of red and blue GCs, demonstrate that the overall patterns are similar, as already noted by B+12. This result argues against a “rejuvenation” of the GC populations that would result in an increase of the higher metallicity red population. B+12 also noted that a minor merger scenario cannot be excluded, but the incoming galaxy should be particularly GC-rich, and that a displacement of the GC population by a galaxy fly-by may be a possible explanation.

The characterization of the distribution of GCs in the radial distance vs $V-I$ space (Section 3.2) demonstrates the lack of a clear bimodality in the color distribution of GCs over the whole interval of radial distances considered in our analysis. Nonetheless, the expected differences of the spatial distributions of red and blue GCs are evident in our analysis, regardless of the specific color value used to separate the two classes (Section 3.1).

While our paper cannot solve the nature of the perturbations in the spatial distribution of GCs in NGC4261, we have contributed detailed 2D maps of the morphology of the asymmetry at different spatial scales. The morphology of the perturbations suggests a stream or an orbiting GC system, but clearly this could also be a projection effect. While difficult to obtain, large kinematic sample of GCs could be used to compare the observed spatial distribution of GCs with the results from simulations of the formation of elliptical galaxies, providing a way to constrain the dynamical evolution of the host galaxy (see, for example Bekki et al. 2005).

5. CONCLUSIONS

We have developed a new approach to the study of the 2D distribution of GCs in elliptical galaxies. The method is an implementation of the KNN method presented in Dressler (1980), supplemented by Monte-Carlo simulations to establish the statistical significance of the results. We have applied this method to NGC4261, a “test galaxy” where significant 2D anisotropy in the GC distribution has been reported (B+12). We confirm that the 2D distribution of GC is not azimuthally isotropic. Moreover, we demonstrate that the 2D distribution departures from the average GC radial distribution results in highly significant spiral-like or broken shell features. While the southern feature is seen in both red and blue GC subsamples, the northern anisotropy shows some evidences of segregation of red and blue GCs. The good characterization of the 2D distribution of GC that we have achieved provides a new benchmark for future simulations of galaxy merging evolution.

R. D’Abrusco gratefully acknowledges the financial support of the US Virtual Astronomical Observatory, which is sponsored by the National Science Foundation

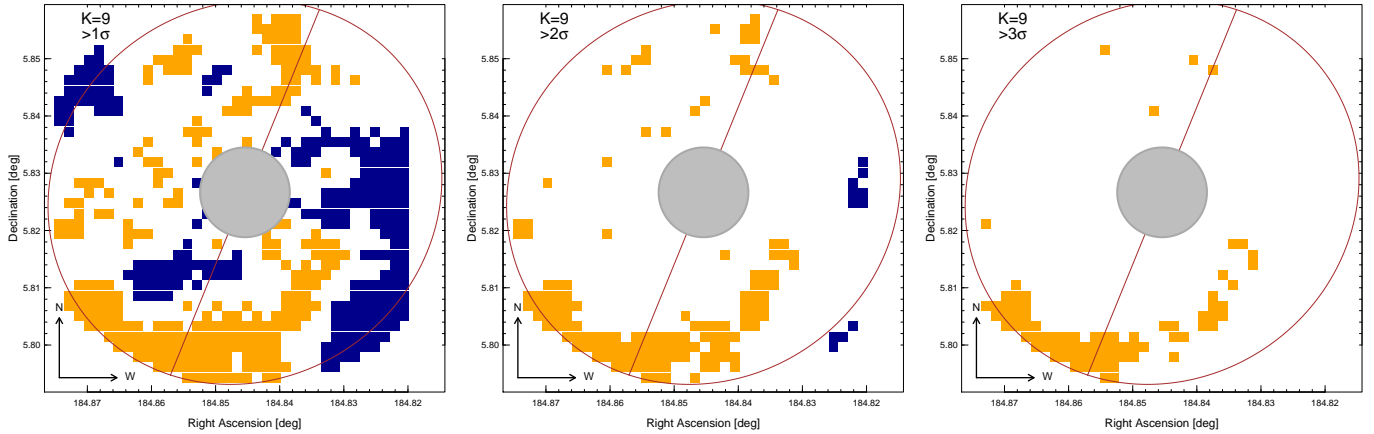


Figure 8. From left to right, positions of the $K=9$ residuals with significance larger than 1σ , 2σ and 3σ .

575 and the National Aeronautics and Space Administration.
 576 TF acknowledges support from the CfA and the ITC
 577 prize fellowship programs. This work was partially sup-
 578 ported by the *Chandra* X-ray Center (CXC), which is
 579 operated by the Smithsonian Astrophysical Observatory
 580 (SAO) under NASA contract NAS8-03060.

REFERENCES

- 581 Bassino, L. P., Faifer, F. R., Forte, J. C., et al. 2006, *A&A*, 451,
 582 789
 583 Bastian, N., Schweizer, F., Goudfrooij, P., Larsen, S. S., &
 584 Kissler-Patig, M. 2013, arXiv:1302.1683
 585 Bekki, K., Forbes, D. A., Beasley, M. A., & Couch, W. J. 2002,
 586 *MNRAS*, 335, 1176
 587 Bekki, K., Beasley, M. A., Brodie, J. P., & Forbes, D. A. 2005,
 588 *MNRAS*, 363, 1211
 589 Binggeli, B., Sandage, A., & Tammann, G. A. 1985, *AJ*, 90, 1681
 590 Blom, C., Spitler, L. R., & Forbes, D. A. 2012, *MNRAS*, 420, 37
 591 Bonfini, P., Zezas, A., Birkinshaw, M., et al. 2012, *MNRAS*, 421,
 592 2872
 593 Brodie, J. P., & Strader, J. 2006, *ARA&A*, 44, 193
 594 de Vaucouleurs, G., de Vaucouleurs, A., Corwin, H. G., Jr., et al.
 595 1991, *S&T*, 82, 621
 596 Dirsch, B., Richtler, T., Geisler, D., et al. 2003, *AJ*, 125, 1908
 597 Dirsch, B., Schuberth, Y., & Richtler, T. 2005, *A&A*, 433, 43
 598 Dressler, A. 1980, *ApJ*, 236, 351
 599 Elmegreen, B. G., Malhotra, S., & Rhoads, J. 2012, *ApJ*, 757, 9
 600 Ferrarese, L., Ford, H. C., & Jaffe, W. 1996, *ApJ*, 470, 444
 601 Forbes, D. A., Spitler, L. R., Strader, J., et al. 2011, *MNRAS*,
 602 413, 2943
 603 Giordano, L., Cortese, L., Trinchieri, G., et al. 2005, *ApJ*, 634,
 604 272
 605 Griffen, B. F., Drinkwater, M. J., Thomas, P. A., Helly, J. C., &
 606 Pimblet, K. A. 2010, *MNRAS*, 405, 375
 607 Hargis, J. R., & Rhode, K. L. 2012, *AJ*, 144, 164
 608 Hernquist, L., & Quinn, P. J. 1988, *ApJ*, 331, 682
 609 Hernquist, L., & Quinn, P. J. 1989, *ApJ*, 342, 1
 610 Lane, R. R., Salinas, R., & Richtler, T. 2013, *A&A*, 549, A148
 611 Muratov, A. L., & Gnedin, O. Y. 2010, *ApJ*, 718, 1266
 612 Peng, E. W., Côté, P., Jordán, A., et al. 2006, *ApJ*, 639, 838
 613 Quinn, P. J. 1984, *ApJ*, 279, 596
 614 Rhode, K. L., & Zepf, S. E. 2001, *AJ*, 121, 210
 615 Rhode, K. L., & Zepf, S. E. 2004, *AJ*, 127, 302
 616 Schweizer, F. 1980, *ApJ*, 237, 303
 617 Strader, J., Romanowsky, A. J., Brodie, J. P., et al. 2011, *ApJS*,
 618 197, 33
 619 Tal, T., van Dokkum, P. G., Nelan, J., & Bezanon, R. 2009, *AJ*,
 620 138, 1417
 621 Tonini, C. 2013, *ApJ*, 762, 39
 622 Wang, Q., Peng, E. W., Blakeslee, J. P., et al. 2013, *ApJ*, 769, 145
 623 Whitmore, B. C., Chandar, R., Schweizer, F., et al. 2010, *AJ*,
 624 140, 75
 625 Zezas, A., Hernquist, L., Fabbiano, G., & Miller, J. 2003, *ApJ*,
 626 599, L73

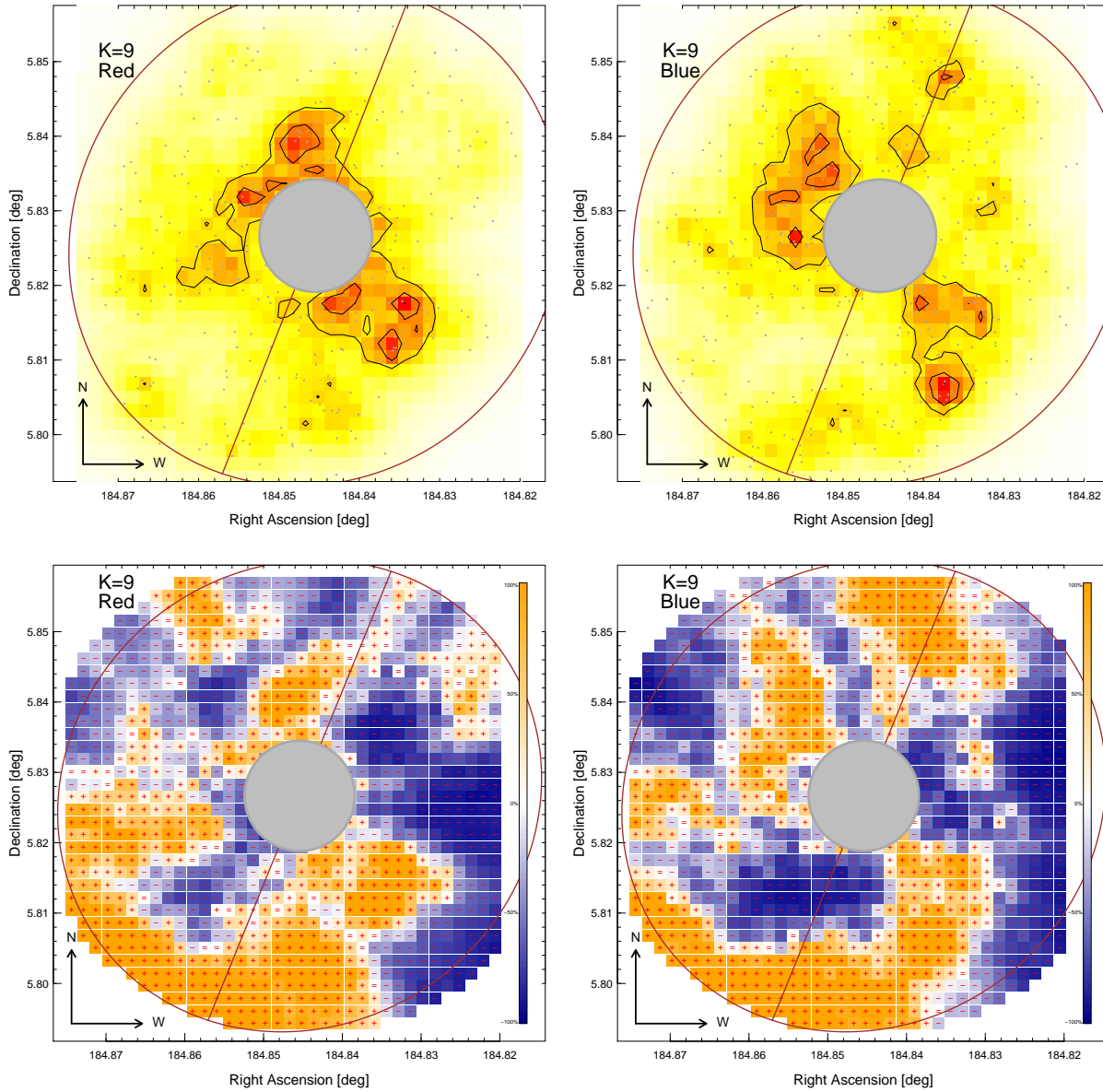


Figure 9. Upper panels: From left to right, observed density maps of red and blue samples for $K=9$. Lower panels: From left to right, residuals maps of red and blue samples obtained for $K=9$. The small +, - and = signs within each pixel indicate positive, negative or null residuals respectively.

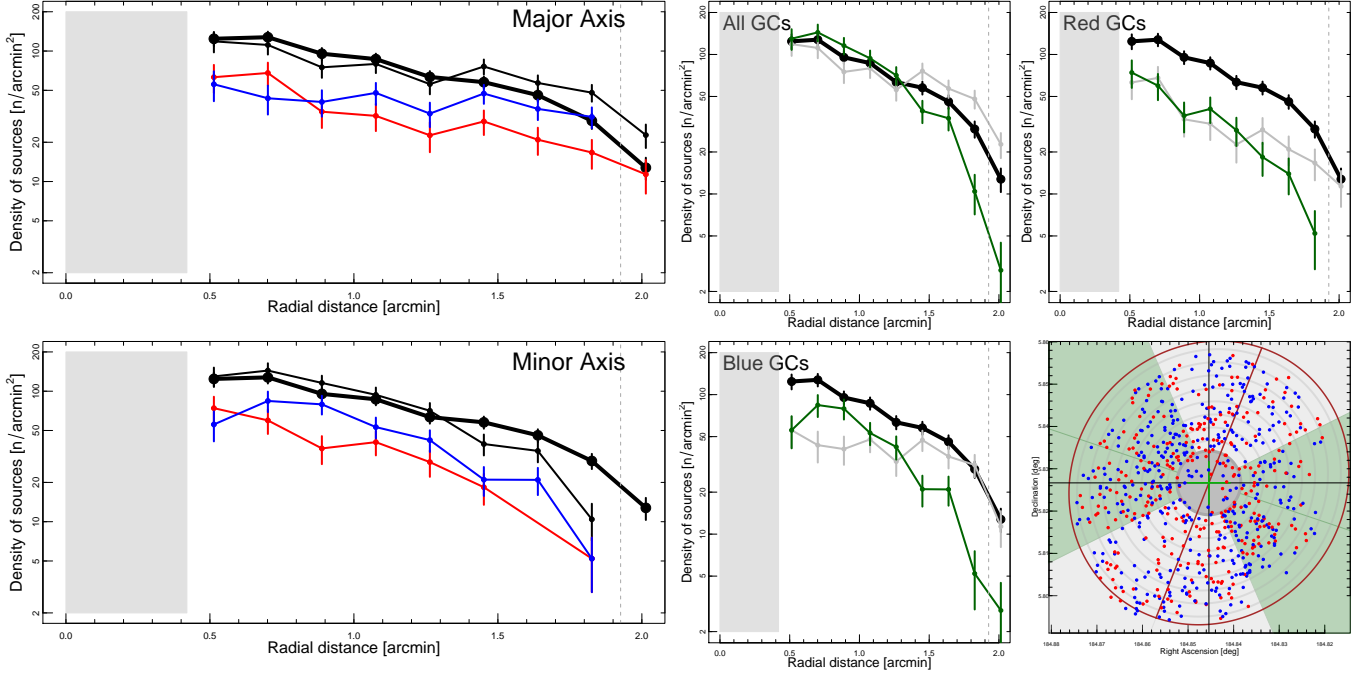


Figure 10. Left: Radial density profiles of all (thin black line), red (red line) and blue (blue line) GCs calculated in elliptical annuli for two azimuthal wedges containing the major and minor axes (upper and lower plot respectively), compared to the overall radial profile of the entire sample (thick black line). Middle and right: observed radial density profiles for different types of GCs in the two regions shown in the lower-right panel. The thick black line represents the radial density profile for all GCs integrated over the whole galaxy. The thin gray and green lines represent the major and minor axis density profiles respectively.

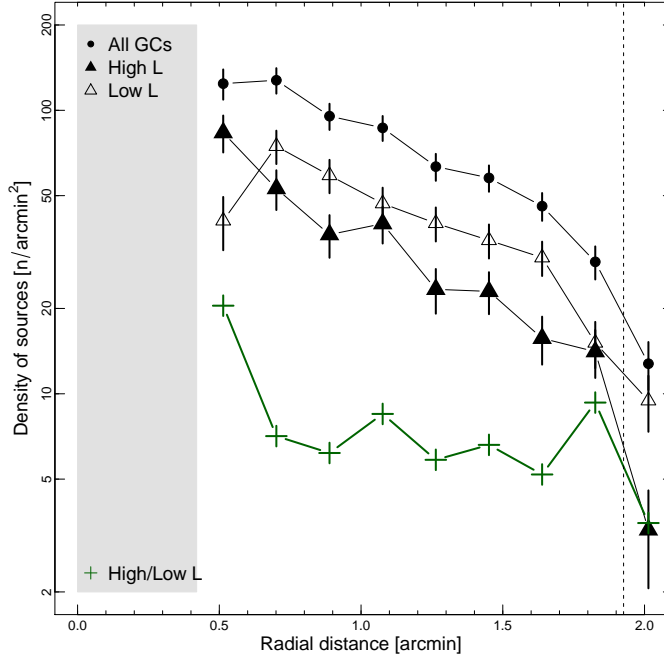


Figure 11. Observed radial density profiles integrated in elliptical annuli for all (solid circles), high-luminosity (solid triangles) and low-luminosity (open triangles) GCs in NGC4261. The green symbols represent the ratio of the high-luminosity to low-luminosity densities profiles, multiplied by 10 for display purposes. In both plots the gray area corresponds to the center of NGC4261 excluded from our analysis where the GC detections are highly incomplete (see (B+12)). The vertical dotted lines represent the major axis of the D_{25} isophote.

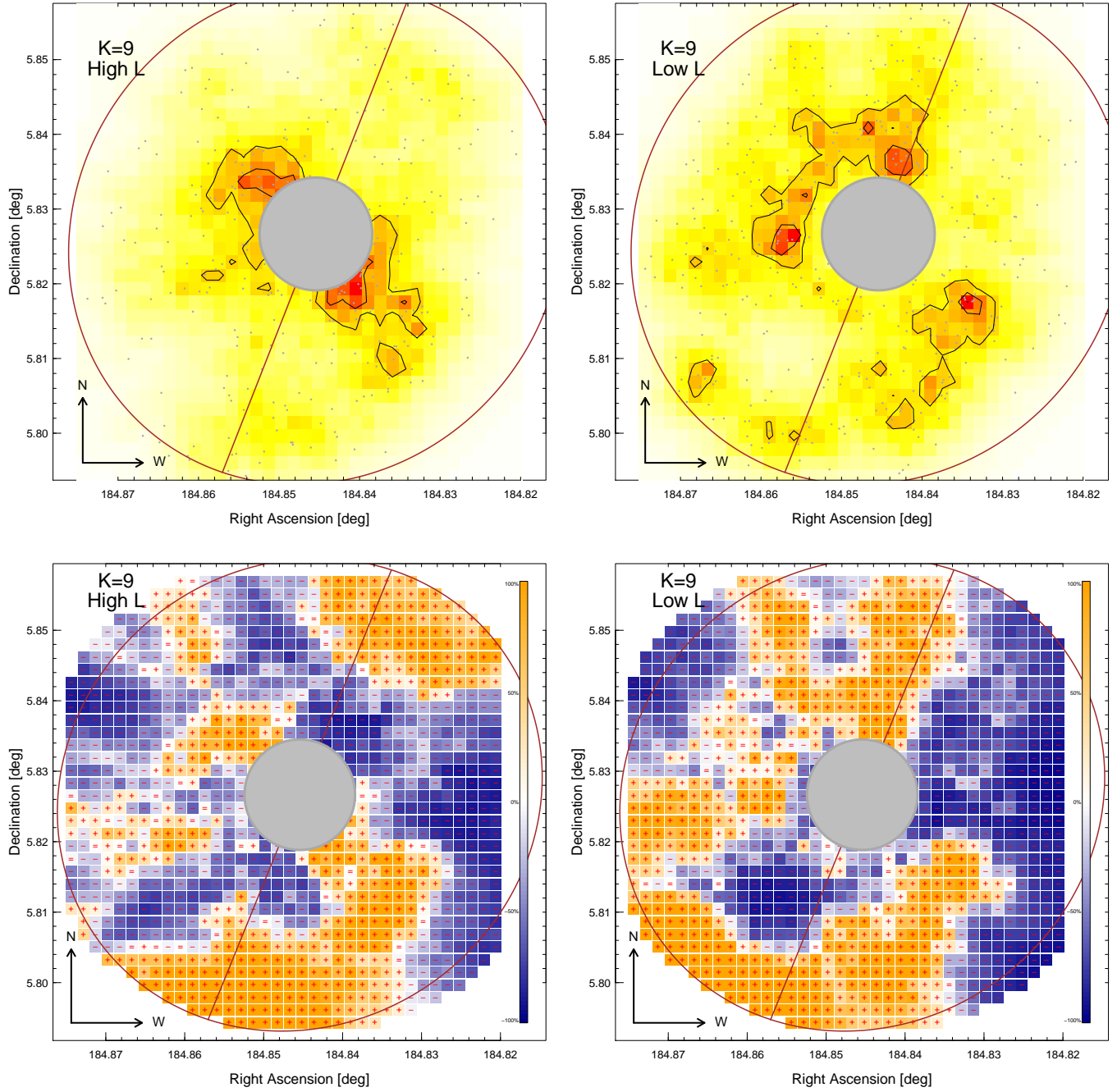


Figure 12. Upper panels: From left to right, $K=9$ density maps derived from the spatial distribution of 316 high-luminosity GCs ($I < 23$) and 402 low-luminosity GCs with $I \geq 23$. Lower panels: From left to right, $K=9$ residual plots of high and low luminosity samples. In both plots the gray area corresponding to the center of NGC4261 excluded from our analysis and the D_{25} elliptical isophote of the galaxy are shown for reference. The small +, - and = signs within each pixel indicate positive, negative or null residuals respectively.

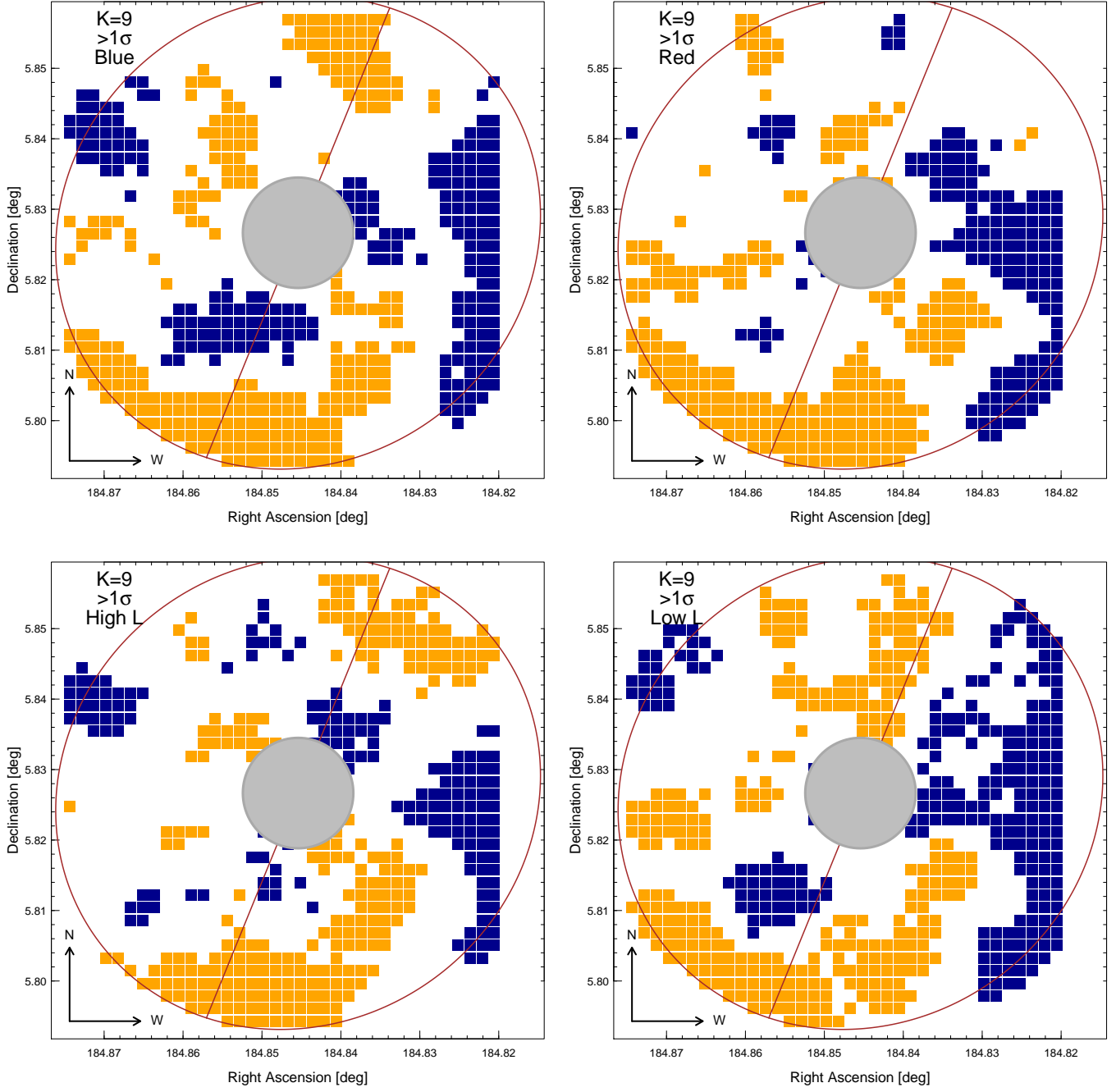


Figure 13. Upper Panels: positions of the $>1\sigma$ residuals for blue (left) and red (right) samples of GCs. Lower panels: positions of the $>1\sigma$ residuals for high-luminosity (left) and low-luminosity (right) samples of GCs. In all plots the gray area corresponding to the center of NGC4261 excluded from our analysis and the D_{25} elliptical isophote of the galaxy are shown for reference.

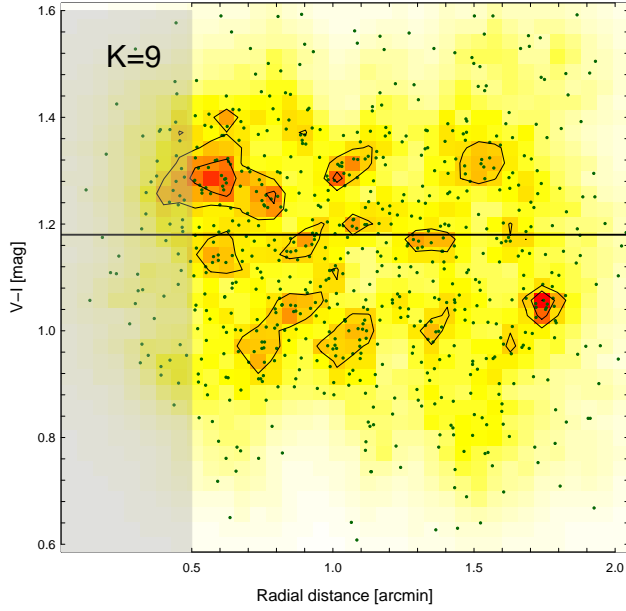


Figure 14. Density map of GCs distribution in the plane generated by the radial distance and the $V-I$ color obtained with the KNN method for $K=9$. The horizontal black line shows the color value used as threshold to separate Red and Blue GCs in this paper. The gray area corresponds to the center of NGC4261 excluded from our analysis. The green points represent the observed positions of the GCs used to determine the density.

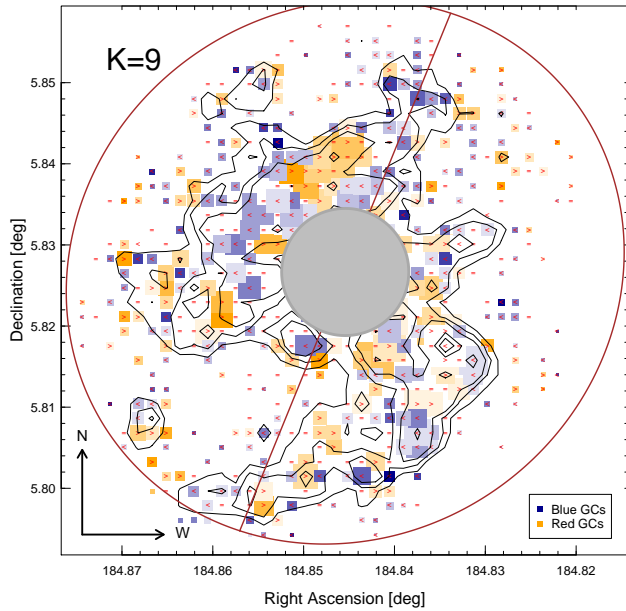


Figure 15. Map of the average color of GCs in pixels. The size of the symbols is proportional to the density of GCs distribution evaluated with the KNN and $K=9$ and the color intensity of the symbols is proportional to the difference between the color threshold value $V-I=1.18$ and the average color of the GCs in each pixel. Small red symbols $>$, $=$ and $<$ are drawn within each pixel with average GCs color $V-I > 1.18$, $V-I = 1.18$ and $V-I < 1.18$ respectively. The isodensity contours reflect the density map with $K=9$ derived from the distribution of all GCs.